

Article

Synthesis and Application Insights of New Phosphate Materials $A_2MnP_2O_7$ (A = Na, K, Li) as Corrosion Inhibitors

Oumaima Moumouche ¹, Hammadi El Harmouchi ¹, Safae Alami ¹, Moussa Ouakki ², Redouane Khaoulaf ³, Khalid Brouzi ⁴, Mohamed Ebn Touhami ¹, Hassane Lgaz ^{5,*}  and Mohamed Harcharras ¹

- ¹ Advanced Materials and Process Engineering Laboratory, Faculty of Sciences, Ibn Tofail University, Kenitra 14000, Morocco; oumaima.moumouche@uit.ac.ma (O.M.); hammadi.elharmouchi@uit.ac.ma (H.E.H.); safae.alami@uit.ac.ma (S.A.); m.ebntouhami@gmail.com (M.E.T.); mharch2009@gmail.com (M.H.)
- ² Organic Chemistry, Catalysis and Environment Laboratory, Faculty of Sciences, Ibn Tofail University, Kenitra 14000, Morocco; moussassaw@gmail.com
- ³ Laboratory of Spectroscopy, Molecular Modeling, Materials, Nanomaterials, Water and Environment, LS3MN2E-CERNE2D, Faculty of Sciences, Mohammed V University, Rabat 10000, Morocco; rkhaoulaf2000@yahoo.fr
- ⁴ Laboratory of Energy, Materials and Sustainable Development (EMDD), Mohammed V University, Rabat 10000, Morocco; k.brouzi@caramail.com
- ⁵ Innovative Durable Building and Infrastructure Research Center, Center for Creative Convergence Education, Hanyang University ERICA, 55 Hanyangdaehak-ro, Sangrok-gu, Ansan-si 15588, Gyeonggi-do, Republic of Korea
- * Correspondence: hlgaz@hanyang.ac.kr or hlgaz@hlgaz.com

Abstract: This study comprehensively characterizes synthesized phosphate materials, specifically $A_2MnP_2O_7$ (where A represents Na, K, or Li), utilizing the X-ray diffraction (XRD) and infrared (IR) spectroscopy techniques. The XRD results corroborate the crystalline nature of these compounds, while the IR spectra disclose pivotal structural characteristics, including the bent geometry of the POP bridge. A significant observation is the mismatch of specific IR bands, suggesting a non-centrosymmetric arrangement in the $A_2MnP_2O_7$ crystal lattice. The synthesized materials were evaluated as corrosion inhibitors for mild steel (MS) in 3 wt.% NaCl. Electrochemical assessments indicate that these materials act as mixed-type inhibitors, demonstrating high inhibition efficiencies ($\eta\%$), reaching peak values of 88.3% for $Na_2MnP_2O_7$, 87% for $K_2MnP_2O_7$, and 86.7% for $Li_2MnP_2O_7$ at a concentration of 10^{-3} mol/L. The study also elucidates the thermodynamic and kinetic parameters dictating the inhibition phenomena. Additionally, scanning electron microscopy (SEM) was employed to examine the surface morphology of mild steel in the presence of these inhibitors.

Keywords: diphosphate; corrosion inhibitor; inorganic inhibitor; mild steel; crystallography; X-ray diffraction; SEM



Citation: Moumouche, O.; El Harmouchi, H.; Alami, S.; Ouakki, M.; Khaoulaf, R.; Brouzi, K.; Ebn Touhami, M.; Lgaz, H.; Harcharras, M. Synthesis and Application Insights of New Phosphate Materials $A_2MnP_2O_7$ (A = Na, K, Li) as Corrosion Inhibitors. *Inorganics* **2024**, *12*, 116. <https://doi.org/10.3390/inorganics12040116>

Academic Editor: Guido KICKELBICK

Received: 8 March 2024

Revised: 29 March 2024

Accepted: 10 April 2024

Published: 16 April 2024



Copyright: © 2024 by the authors. Licensee MDPI, Basel, Switzerland. This article is an open access article distributed under the terms and conditions of the Creative Commons Attribution (CC BY) license (<https://creativecommons.org/licenses/by/4.0/>).

1. Introduction

Alkali metal phosphates, with their diverse structural arrangements and tunable properties, represent a fascinating class of materials with widespread technological implications. These phosphates, described by the general formula $A(MP_2O_7)$ or $A_2(MP_2O_7)$ (where A represents an alkali metal and M denotes a transition metal), encompass a broad spectrum of compounds finding applications in fields as varied as scintillation for radiation detection [1,2], phosphors for lighting [3], solid-state lasers [4], catalytic processes, and ionic conductors [5]. Their structural adaptability stems from the fundamental building blocks of corner-sharing MO_4 tetrahedra and four distinct (P_2O_7) groups, which assemble into layered architectures capable of accommodating monovalent alkali metal ions (A) within the interlayer spaces [6]. This structural flexibility gives rise to remarkable variations in optical, magnetic, electrical, and catalytic properties, making alkali metal phosphates highly attractive for fundamental research and practical applications.

Mild steel, a low-carbon form of steel, is a versatile and widely used engineering material thanks to its affordability, strength, and ease of fabrication. It finds applications in construction, automotive manufacturing, pipelines, and various industrial equipment. However, a major drawback of mild steel is its susceptibility to corrosion in different environments [7–10]. In the presence of moisture, oxygen, and electrolytes, mild steel readily oxidizes, leading to rust formation and the degradation of its structural integrity. This corrosion can be further accelerated in acidic or alkaline solutions, saltwater environments, and under conditions of elevated temperature or stress, posing significant challenges for the long-term use of mild steel components [11–13].

One of the most compelling challenges in materials science is the development of effective strategies to combat corrosion, a pervasive and costly degradation process affecting metals and alloys exposed to various environments [14–17]. The economic consequences of corrosion are staggering, with global costs estimated to be in the trillions of dollars annually. Corrosion inhibitors offer a practical and efficient approach to mitigating the detrimental effects of corrosion [6]. When judiciously incorporated into a susceptible system, these substances significantly reduce the rate of material deterioration [6]. An especially critical application of corrosion inhibitors lies in the protection of steel reinforcements embedded within concrete structures, where premature corrosion represents a severe threat to structural integrity [18–20]. Corrosion inhibitors protect metal surfaces by adsorbing onto the metal and forming a protective barrier that hinders the corrosive interaction with the environment. This adsorption can occur through physical interactions (physisorption), chemical bond formation (chemisorption), or a combination of both mechanisms. Physisorption relies on weaker forces like van der Waals interactions and is often reversible. Chemisorption involves electron transfer or sharing, resulting in strong, irreversible bonds with the metal surface, offering more robust protection. Understanding the dominant adsorption mechanism is crucial, as it influences inhibitor stability and the impact of environmental factors, and provides guidance for designing new, more effective corrosion inhibitors with tailored structures.

Among the wide array of corrosion inhibitors explored to date, phosphates have garnered considerable interest due to their favorable combination of cost-effectiveness, low toxicity, and environmental compatibility [21,22]. The past two decades have witnessed a surge in research endeavors aimed at elucidating the mechanisms of phosphate-based corrosion inhibition and optimizing their performance in both simulated pore solutions and real-world applications [23]. The efficacy of phosphates as corrosion inhibitors likely stems from the formation of protective surface films that hinder the corrosive interaction between the underlying metal and its environment.

A growing body of literature underscores the potential of phosphate-based materials to combat corrosion in diverse settings. Bastidas et al. pioneered a comparative study evaluating the performance of sodium monofluorophosphate ($\text{Na}_2\text{PO}_3\text{F}$), disodium hydrogen phosphate (Na_2HPO_4), and trisodium phosphate (Na_3PO_4) as corrosion inhibitors for steel embedded in mortar [24]. Within this system, $\text{Na}_2\text{PO}_3\text{F}$ exhibited superior inhibition efficiency compared to the other phosphate compounds. More recently, Elhafiane et al. synthesized a novel nickel potassium phosphate, $\text{NiK}_{1.18}\text{N}_{0.82}(\text{H}_2\text{P}_2\text{O}_7)_2 \cdot 2\text{H}_2\text{O}$ (BP), and demonstrated its ability to inhibit the corrosion of mild steel in 1 M HCl solution [25]. Furthermore, Khmiyas explored the use of $\text{AgSrCu}_{4.5}(\text{PO}_4)_6$ as a corrosion inhibitor for C35E steel in an acidic medium and unveiled the influence of temperature on the underlying inhibition mechanisms [26].

Motivated by the promising findings in the field of phosphate-based corrosion inhibition, this study focuses on the synthesis of the $\text{A}_2\text{MnP}_2\text{O}_7$ series of compounds (where A = Li, Na, K) using a dry synthesis method. These materials are subsequently subjected to meticulous characterization employing X-ray diffraction, FT-IR, and Raman spectroscopy to establish their structural features and vibrational properties. Crucially, this work investigates their potential as corrosion inhibitors for mild steel in a 3 wt.% NaCl solution

through comprehensive electrochemical measurements and in-depth surface analysis using scanning electron microscopy (SEM).

2. Results and Discussion

2.1. X-ray Diffraction

The X-ray diffraction (XRD) patterns presented in Figure 1 provide compelling evidence for the successful synthesis of the target compounds $\text{K}_2\text{MnP}_2\text{O}_7$, $\text{Na}_2\text{MnP}_2\text{O}_7$, and $\text{Li}_2\text{MnP}_2\text{O}_7$. A detailed analysis reveals that both $\text{K}_2\text{MnP}_2\text{O}_7$ and $\text{Li}_2\text{MnP}_2\text{O}_7$ crystallize in the monoclinic system, as supported by their agreement with the reference patterns JCPDS n° 810-4021 and JCPDS n° 100-8658, respectively. In contrast, $\text{Na}_2\text{MnP}_2\text{O}_7$ exhibits a triclinic crystal structure, aligning well with JCPDS n° 201-239.

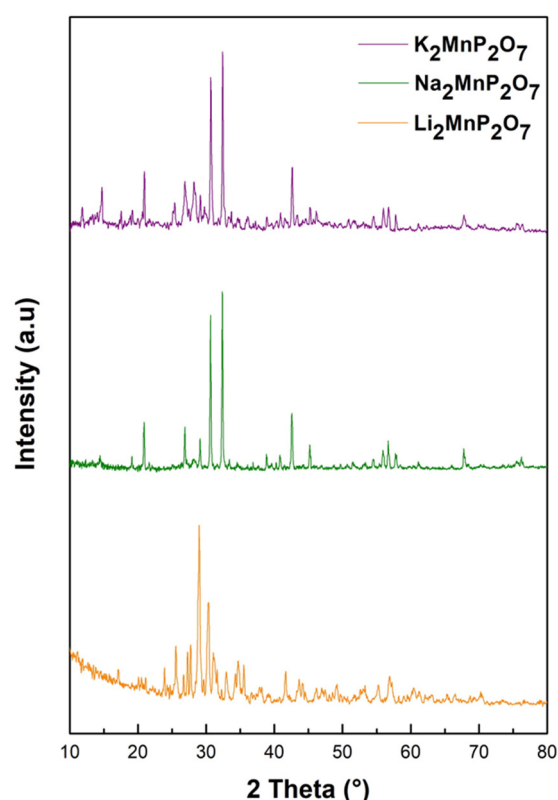


Figure 1. XRD spectra of different compounds.

These findings offer valuable insights into the structural characteristics of the synthesized compounds. The distinct crystal systems (monoclinic and triclinic) suggest variations in atomic arrangements and lattice parameters, potentially leading to differences in their physical and chemical properties.

2.2. Spectroscopic Evaluation of $A_2\text{MnP}_2\text{O}_7$ ($A = \text{Li}, \text{Na}, \text{K}$)

The infrared (IR) absorption and Raman scattering spectra of the synthesized diphosphates $A_2\text{MnP}_2\text{O}_7$ ($A = \text{Li}, \text{Na}, \text{K}$) provide valuable insights into their vibrational modes and structural characteristics (Figure 2). A careful analysis of the spectra reveals three distinct frequency ranges. The high-frequency region ($1001\text{--}1183\text{ cm}^{-1}$) features prominent Raman bands for $\text{K}_2\text{MnP}_2\text{O}_7$, $\text{Na}_2\text{MnP}_2\text{O}_7$, and $\text{Li}_2\text{MnP}_2\text{O}_7$, consistent with their crystalline nature. Notably, the exceptionally sharp bands observed for $\text{Na}_2\text{MnP}_2\text{O}_7$ suggest a higher degree of crystallinity. This region reveals characteristic bands for each compound, such as the $1001\text{--}1137\text{ cm}^{-1}$ series for $\text{K}_2\text{MnP}_2\text{O}_7$ and distinct peaks at 740 , 732 , and 787 cm^{-1} for $\text{Na}_2\text{MnP}_2\text{O}_7$. These spectral features likely arise from the stretching vibrations of the P-O-P bridges and terminal PO_3 groups within the diphosphate framework.

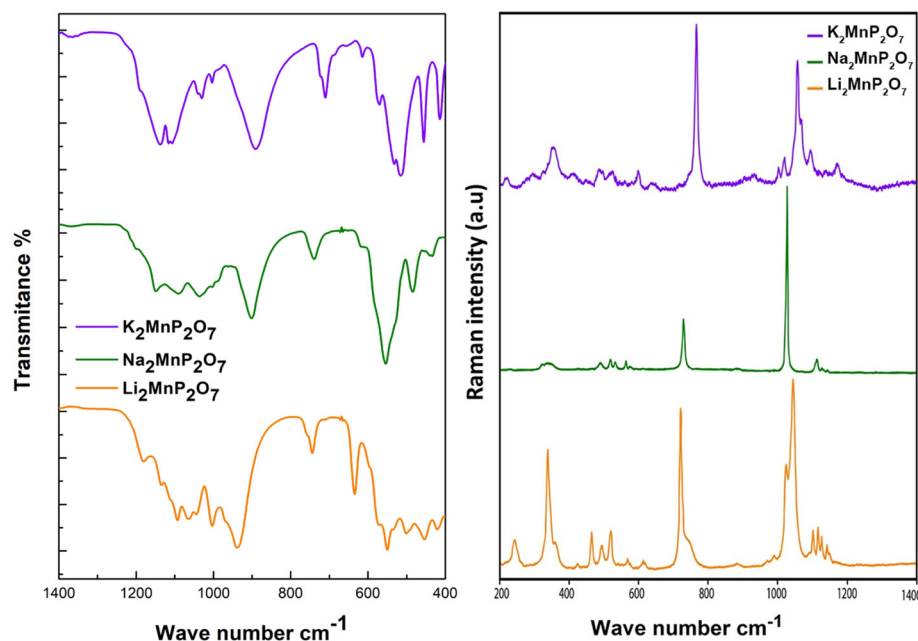


Figure 2. Infrared and Raman spectra of $A_2MnP_2O_7$ ($A = Li, Na, K$).

The mid-frequency region ($700\text{--}950\text{ cm}^{-1}$) encompasses the symmetric and asymmetric stretching vibrations of P-O-P linkages. Examining both IR and Raman spectra within this range offers a more comprehensive understanding of these vibrational modes. Finally, the low-frequency region ($200\text{--}700\text{ cm}^{-1}$) primarily reflects the deformation modes (δPO_3) of the phosphate groups, with potential contributions from lattice vibrations and Mn-O bonds. The lack of coincidental bands in the IR and Raman spectra for $A_2MnP_2O_7$ ($A = Li, Na, K$) strongly indicates a centrosymmetric crystal lattice, a finding consistent with the X-ray diffraction analysis. For clarity, Table 1 summarizes the key IR and Raman band assignments.

Table 1. Attribution of bands for infrared and Raman spectra corresponding to $A_2MnP_2O_7$ ($A = Li, Na, K$).

$K_2MnP_2O_7$		$Na_2MnP_2O_7$		$Li_2MnP_2O_7$		Attribution
IR (cm^{-1})	Ra (cm^{-1})	IR (cm^{-1})	Ra (cm^{-1})	IR (cm^{-1})	Ra (cm^{-1})	
1137	1175	1148	1152	1183	1182	$U^{as}PO_3$ U^sPO_3
1108	1150	1087	1141	1135	1163	
1028	1120	1038	1130	1094	1104	
1001	1112		1027	1063	1084	
	1105			1041	1035	
	1024			1000	1021	
	1013					
	983					
888	891	905	902	937	942	$U^{as}POP$
710	740	743	732	745	787	U^sPOP
612	603	618	592	635	632	δPO_3
568	582	555	583	572	604	
535	506	484	543	550	591	
515	493	432	522	502	531	
460	460		490	454	524	
455	409		335	420	516	
414	370		249		483	
	260				424	
					411	
					354	
					332	
					302	
					221	

2.3. Corrosion Inhibition Studies

2.3.1. Open Circuit Potential (OCP) Measurements

The open circuit potential (OCP) and its temporal evolution in a 3 wt.% NaCl aqueous medium were meticulously investigated both before and after the addition of various concentrations of $\text{Na}_2\text{MnP}_2\text{O}_7$, $\text{K}_2\text{MnP}_2\text{O}_7$, and $\text{Li}_2\text{MnP}_2\text{O}_7$ compounds, following a half-hour immersion at 298 K. These observations are presented in Figure 3. Notably, the introduction of these compounds into the solution induces a discernible shift in the corrosion potential (E_{corr}) towards more negative values when contrasted with the baseline solution devoid of these additives. This shift is indicative of the influence exerted by the presence of the examined species, suggesting a modification in the electrochemical environment at the metal–solution interface.

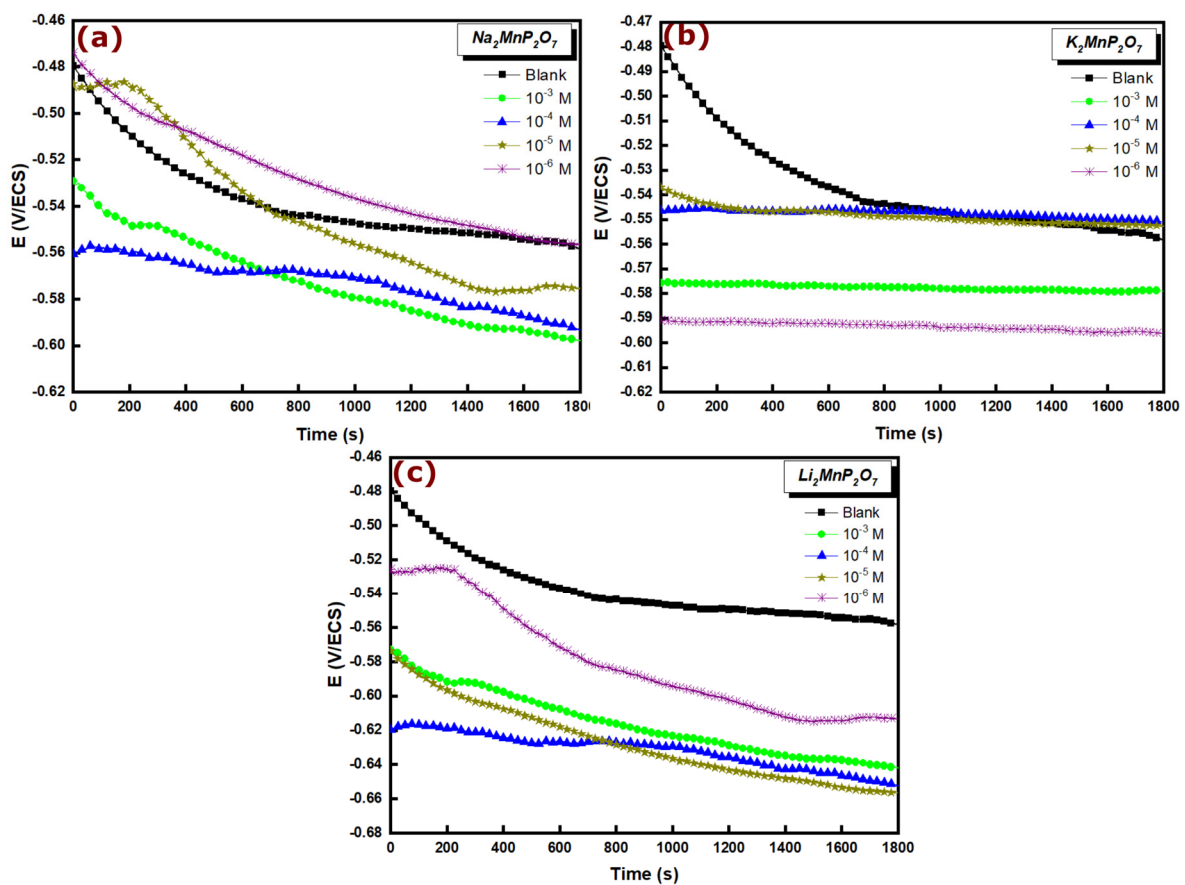


Figure 3. Open circuit potential (OCP) and its evolution with time in NaCl 3% medium before and after adding various concentrations of (a) $\text{Na}_2\text{MnP}_2\text{O}_7$, (b) $\text{K}_2\text{MnP}_2\text{O}_7$, and (c) $\text{Li}_2\text{MnP}_2\text{O}_7$ at 298 K.

2.3.2. Potentiodynamic Polarization Curves

The inhibition efficiency of the synthesized phosphate compounds for mild steel in 3 wt.% NaCl was investigated by systematically varying their concentration from 10^{-6} to 10^{-3} M. Figure 4 illustrates the polarization curves of mild steel in 3 wt.% NaCl at 298 K, both with and without the addition of these phosphate inhibitors at various concentrations. The polarization curves reveal a decrease in current density upon the addition of $\text{Na}_2\text{MnP}_2\text{O}_7$, $\text{K}_2\text{MnP}_2\text{O}_7$, and $\text{Li}_2\text{MnP}_2\text{O}_7$, with both the cathodic and anodic branches shifting downwards. This suppressive effect on the current density becomes more pronounced as the concentration of the phosphate inhibitors is increased from 10^{-6} to 10^{-3} M. Furthermore, the potential difference between the E_{corr} of blank solutions and those of inhibited solutions remains within 85 mV, indicating that $\text{Na}_2\text{MnP}_2\text{O}_7$, $\text{K}_2\text{MnP}_2\text{O}_7$, and $\text{Li}_2\text{MnP}_2\text{O}_7$ function as mixed-type inhibitors [21].

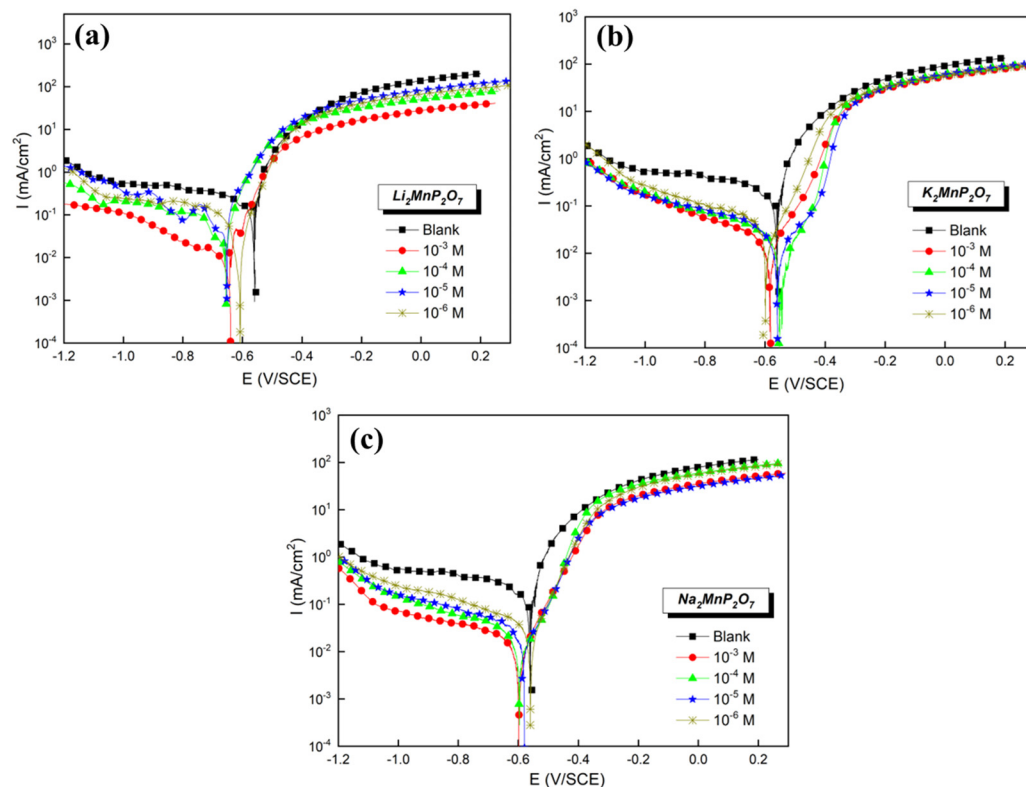


Figure 4. Polarization curves at 298 K of mild steel with and without the addition of (a) $\text{Li}_2\text{MnP}_2\text{O}_7$, (b) $\text{K}_2\text{MnP}_2\text{O}_7$, and (c) $\text{Na}_2\text{MnP}_2\text{O}_7$ at varying concentrations in 3 wt.% NaCl.

Table 2 summarizes the electrochemical parameters derived from the polarization curves, including corrosion potential (E_{corr}) and corrosion current density (i_{corr}). The data demonstrate that the tested phosphate-based compounds effectively inhibit corrosion in a 3 wt.% NaCl medium. This effectiveness is reflected in the significantly reduced corrosion current densities and high inhibition efficiencies [27,28].

Table 2. Electrochemical parameters of the polarization diagram of mild steel in 3 wt.% NaCl solution with and without the addition of different compounds at different concentrations.

Compounds	C (M)	$-E_{\text{corr}}$ mV/ECS	i_{corr} $\mu\text{A cm}^{-2}$	η (%)
Blank	-	559	464	-
$\text{Li}_2\text{MnP}_2\text{O}_7$	10^{-3}	641	62	86.6
	10^{-4}	653	126	72.8
	10^{-5}	657	212	54.3
	10^{-6}	614	265	42.9
$\text{K}_2\text{MnP}_2\text{O}_7$	10^{-3}	580	60	87.0
	10^{-4}	551	65	85.9
	10^{-5}	553	78	83.2
	10^{-6}	597	84	81.9
$\text{Na}_2\text{MnP}_2\text{O}_7$	10^{-3}	597	54	88.3
	10^{-4}	594	76	83.6
	10^{-5}	577	90	80.6
	10^{-6}	557	103	77.8

The inhibition efficiency ($\eta\%$) is calculated using the following equation:

$$\eta (\%) = \frac{i_0 - i}{i_0} \times 100 \quad (1)$$

where i_0 and i represent the corrosion current densities without and with the inhibitor, respectively.

At the highest tested concentration of 10^{-3} M, the inhibition efficiencies for $\text{Na}_2\text{MnP}_2\text{O}_7$, $\text{K}_2\text{MnP}_2\text{O}_7$, and $\text{Li}_2\text{MnP}_2\text{O}_7$ reach 88.3%, 87%, and 86.6%, respectively.

2.3.3. Electrochemical Impedance Spectroscopy

Figure 5 presents the Nyquist diagrams obtained for mild steel immersed in 3 wt.% NaCl, with and without the addition of the $\text{A}_2\text{MnP}_2\text{O}_7$ compounds at varying concentrations. The Nyquist plots exhibit two incomplete capacitive loops. The high-frequency loop corresponds to the protective film formed on the electrode surface, while the low-frequency loop is attributed to the charge transfer reaction. Notably, the diameter of the capacitive loops increases with increasing $\text{A}_2\text{MnP}_2\text{O}_7$ concentration, suggesting the formation of a more robust inhibitor film on the metal surface [29].

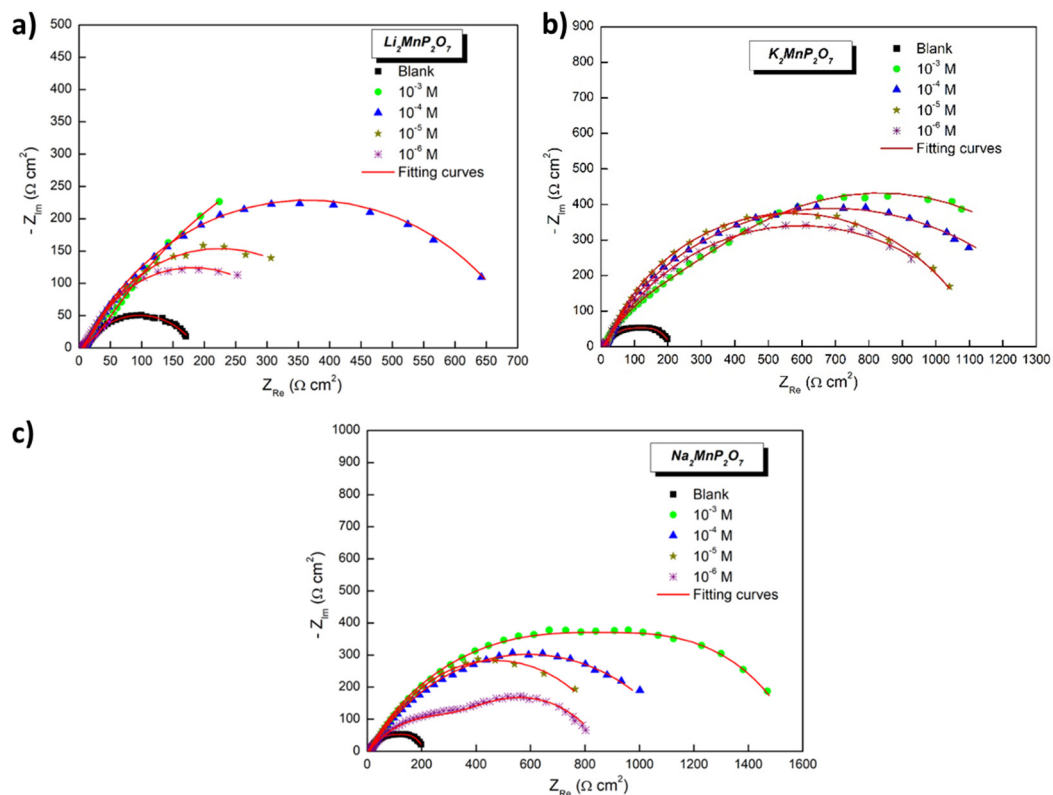


Figure 5. Nyquist plots of mild steel in 3 wt.% NaCl solutions with different concentrations of (a) $\text{Li}_2\text{MnP}_2\text{O}_7$, (b) $\text{K}_2\text{MnP}_2\text{O}_7$, and (c) $\text{Na}_2\text{MnP}_2\text{O}_7$ compounds at 298 K.

This observation is further supported by the Bode plots (Figure 6), which depict the impedance response in the absence and presence of different $\text{A}_2\text{MnP}_2\text{O}_7$ ($A = \text{Li}, \text{Na}, \text{K}$) concentrations.

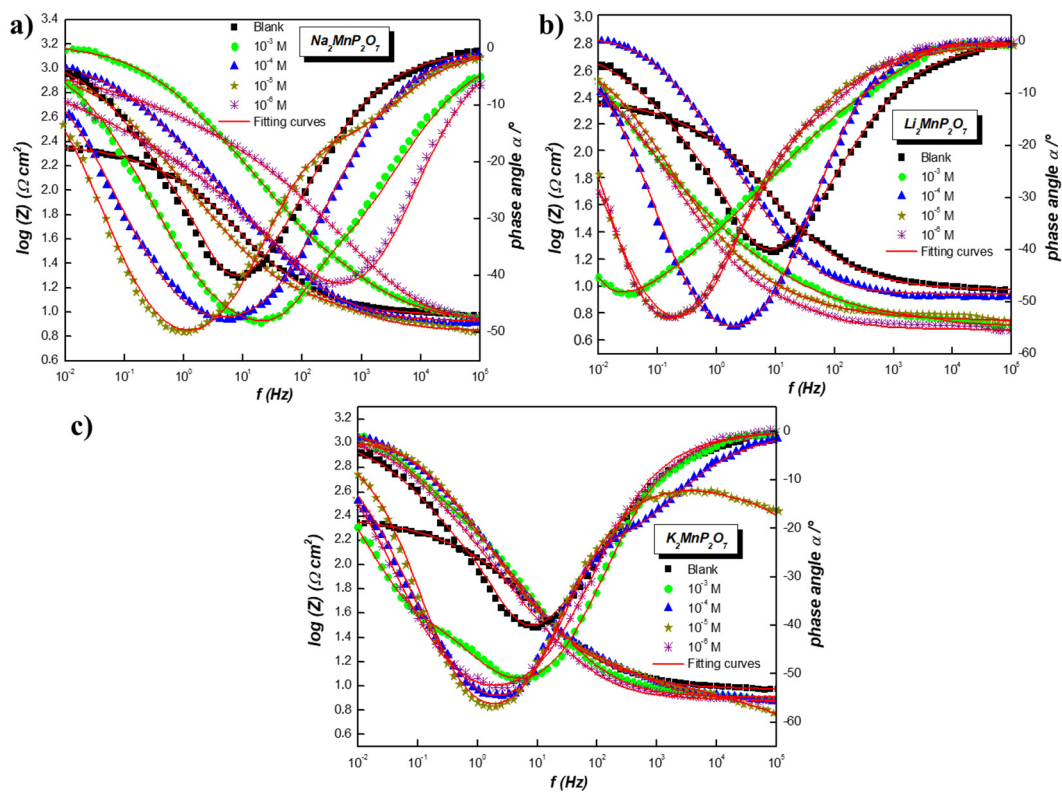


Figure 6. Bode plots of (a) $\text{Na}_2\text{MnP}_2\text{O}_7$, (b) $\text{Li}_2\text{MnP}_2\text{O}_7$ and (c) $\text{K}_2\text{MnP}_2\text{O}_7$, and at different concentrations in the absence and presence of 3 wt.% NaCl at 298 K.

To gain a quantitative understanding of the EIS data, an electrical equivalent circuit (EEC, Figure 7) was employed to model the electrochemical behavior. In this circuit, R_s denotes the solution resistance, R_{ct} represents the charge transfer resistance, and R_f signifies the film resistance. The constant phase elements (CPEs) CPE_f and CPE_{dl} represent the film capacitance and double-layer capacitance, respectively. The use of CPEs accounts for non-ideal behavior arising from surface inhomogeneities [30].

The impedance of a constant phase element is given by the following equation (Equation (2)):

$$Z_{\text{CPE}}(\omega) = Q^{-1}(j\omega)^{-n} \quad (2)$$

where Q is the CPE constant, ω is the angular frequency, j is the imaginary unit, and n is the CPE exponent ($0 \leq n \leq 1$).

Brug's equation calculates the effective double-layer ($C_{\text{eff},dl}$, Equation (3)) and film ($C_{\text{eff},f}$, Equation (4)) capacitances using the constant phase element (CPE) parameters Q and n , the solution resistance (R_s), and the polarization resistance (R_p) [30]:

$$C_{\text{eff},dl} = Q_{dl}^{1/n} \times \left(\frac{1}{R_s} + \frac{1}{R_p} \right)^{\frac{n-1}{n}} \quad (3)$$

$$C_{\text{eff},f} = Q_f^{1/n} \times \left(R_f \right)^{\frac{1-n}{n}} \quad (4)$$

The analysis of the EEC fitting parameters reveals important trends. The decrease in Q_{ct} values with an increasing inhibitor concentration implies the formation of a protective layer at the metal–solution interface, likely due to the displacement of pre-absorbed water molecules [31]. This adsorption of $\text{Na}_2\text{MnP}_2\text{O}_7$, $\text{K}_2\text{MnP}_2\text{O}_7$, and $\text{Li}_2\text{MnP}_2\text{O}_7$ on the metal surface leads to a reduction in the electrical capacitance. An increase in inhibitor concentration was directly correlated with a decrease in effective double-layer capacitance ($C_{\text{eff},dl}$) values when compared to the blank solution. This substantial capacitance decrease

suggests the adsorption of inhibitor molecules onto the metal surface, resulting in a thicker double electric layer [32].

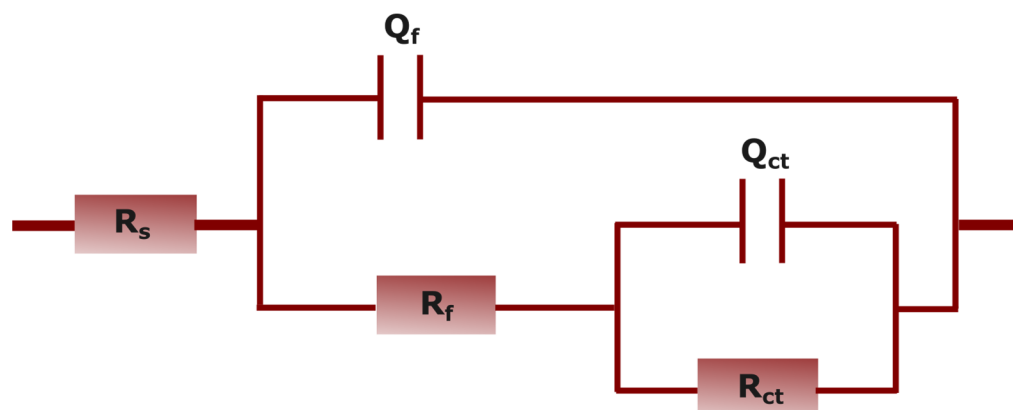


Figure 7. Equivalent circuit for adjusting the EIS of mild steel in the presence of $\text{Na}_2\text{MnP}_2\text{O}_7$, $\text{K}_2\text{MnP}_2\text{O}_7$, and $\text{Li}_2\text{MnP}_2\text{O}_7$.

The polarization resistance (R_p) is calculated as follows:

$$R_p = R_{ct} + R_f \quad (5)$$

Table 3 highlights a significant increase in R_p values as the inhibitor concentration rises. This observation strongly supports the hypothesis that the adsorption of $\text{Na}_2\text{MnP}_2\text{O}_7$, $\text{K}_2\text{MnP}_2\text{O}_7$, and $\text{Li}_2\text{MnP}_2\text{O}_7$ molecules onto the mild steel surface enhances corrosion resistance.

Table 3. Electrochemical impedance parameters extracted from EEC for mild steel in the absence and presence of inhibitors in 3 wt.% NaCl at 298 K.

C (M)	R_s ($\Omega \text{ cm}^2$)	R_f ($\Omega \text{ cm}^2$)	n_f	Q_f ($\mu\text{F}/\text{cm}^2$)	$C_{\text{eff},f}$ ($\mu\text{F}/\text{cm}^2$)	R_{ct} ($\Omega \text{ cm}^2$)	n_{ct}	Q_{ct} ($\mu\text{F}/\text{cm}^2$)	$C_{\text{eff},dl}$ ($\mu\text{F}/\text{cm}^2$)	R_p ($\Omega \text{ cm}^2$)	$\eta\%$
3 wt.% NaCl	10.2	161.0	0.705	1399	750	38.0	0.99	1451	1387	199.0	-
$\text{Li}_2\text{MnP}_2\text{O}_7$											
10^{-3}	5.8	260	0.603	1618	915	1091	0.731	678	88.15	1351	85.3
10^{-4}	8.6	148	0.728	1297	700	562	0.729	935	154.76	710	72.0
10^{-5}	6.5	51	0.811	1704	964	376	0.813	1047	330.95	427	53.4
10^{-6}	5.4	32	0.812	1845	958	314	0.805	1124	325.06	346	42.5
$\text{K}_2\text{MnP}_2\text{O}_7$											
10^{-3}	8.0	637	0.683	341	168	866	0.786	283	53.76	1503	86.7
10^{-4}	6.7	229	0.675	1121	582	1150	0.901	196	94.48	1379	85.5
10^{-5}	8.5	137	0.714	1129	535	1003	0.992	219	208.16	1140	82.5
10^{-6}	7.6	250	0.667	1024	519	827	0.652	359	15.29	1077	81.5
$\text{Na}_2\text{MnP}_2\text{O}_7$											
10^{-3}	3.4	1261	0.641	397	269	335	0.890	641	300.15	1596	87.5
10^{-4}	8.8	886	0.609	499	295	284	0.923	759	498.50	1170	83.0
10^{-5}	7.8	615	0.694	684	467	380	0.954	586	451.48	995	80.0
10^{-6}	1.2	440	0.641	837	478	428	0.686	473	15.43	868	77.0

2.3.4. Analysis of Adsorption Isotherms

Adsorption isotherms offer crucial insights into the nature of the interaction between inhibitors and the mild steel surface. Several adsorption isotherm models, including Langmuir, Temkin, Freundlich, and Frumkin, were evaluated to describe the adsorption behavior of the corrosion inhibitors in this study [33]. The analysis of the curves in

Figure 8 reveals that the adsorption of the inorganic inhibitors $\text{Na}_2\text{MnP}_2\text{O}_7$, $\text{K}_2\text{MnP}_2\text{O}_7$, and $\text{Li}_2\text{MnP}_2\text{O}_7$ onto the mild steel surface can be best described by the Langmuir isotherm model. This model is expressed by the following equation:

$$\frac{\theta}{1 - \theta} = K_{ads} C_{inh} \quad (6)$$

where θ represents the surface coverage, K_{ads} is the equilibrium adsorption constant, and C_{inh} denotes the equilibrium inhibitor concentration. A plot of C_{inh}/θ versus C_{inh} yields a slope close to unity, further validating the applicability of the Langmuir adsorption model.

The strong linear correlations (correlation coefficients approaching 1) affirm that the adsorption of $\text{Na}_2\text{MnP}_2\text{O}_7$, $\text{K}_2\text{MnP}_2\text{O}_7$, and $\text{Li}_2\text{MnP}_2\text{O}_7$ derivatives on mild steel in a 3 wt.% NaCl medium adheres to the Langmuir adsorption isotherm (Figure 8).

Table 4 presents the thermodynamic parameters of adsorption derived from the K_{ads} values using the following relationships [34]:

$$\Delta G_{ads} = -RT \ln (55.5 K_{ads}) \quad (7)$$

where ΔG_{ads} is the standard adsorption free energy, R is the universal gas constant, T is the absolute temperature, and 55.5 represents the molar concentration of water in the solution.

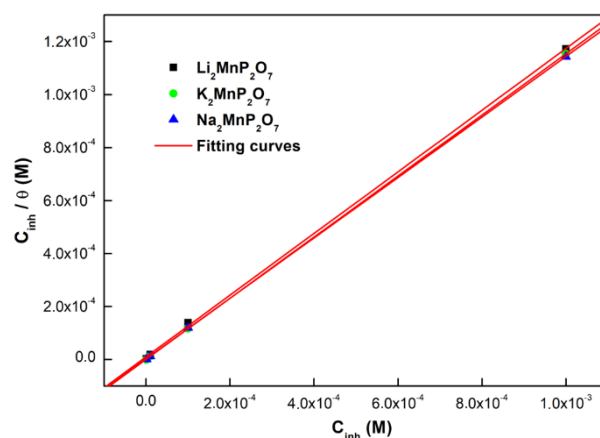


Figure 8. Langmuir adsorption model for mild steel in 3 wt.% NaCl at 298 K in the presence of $\text{Na}_2\text{MnP}_2\text{O}_7$, $\text{K}_2\text{MnP}_2\text{O}_7$, and $\text{Li}_2\text{MnP}_2\text{O}_7$.

Table 4. Thermodynamic parameters for the adsorption of the two compounds on mild steel surface in 3 wt.% NaCl at 298 K.

Medium (3 wt. % NaCl)	K_{ads} (L/mol)	ΔG_{ads} (Kj/mol)	R^2	Slopes
$\text{Li}_2\text{MnP}_2\text{O}_7$	$101.5 \cdot 10^3$	−38.5	0.999	1.16
$\text{K}_2\text{MnP}_2\text{O}_7$	$315.1 \cdot 10^4$	−47.0	1	1.15
$\text{Na}_2\text{MnP}_2\text{O}_7$	$412.8 \cdot 10^3$	−42.0	0.9999	1.14

The ΔG_{ads} values consistently below -40 kJ mol^{-1} provide compelling evidence for chemisorption as the dominant adsorption mechanism. This type of adsorption likely involves charge sharing or electron transfer between the inhibitor molecules and the iron atoms on the metal surface [35]. For $\text{Li}_2\text{MnP}_2\text{O}_7$, the calculated ΔG_{ads} values fall within the range of -20 to -40 kJ mol^{-1} , suggesting that the molecules can interact with the mild steel surface through both physisorption and chemisorption processes [36,37]. In contrast, the ΔG_{ads} values for $\text{K}_2\text{MnP}_2\text{O}_7$ and $\text{Na}_2\text{MnP}_2\text{O}_7$ both exceed -40 kJ mol^{-1} , unequivocally indicating chemisorption as the primary mechanism for their adsorption onto the mild steel surface.

2.3.5. Temperature Effect on the Inhibition Behavior

Temperature plays a crucial role in influencing the behavior of materials in corrosive environments, including the interactions between metals and inhibitors [38,39]. To investigate the temperature dependence of the inhibition efficiency of $\text{Na}_2\text{MnP}_2\text{O}_7$, $\text{K}_2\text{MnP}_2\text{O}_7$, and $\text{Li}_2\text{MnP}_2\text{O}_7$, electrochemical measurements were conducted between 298 K and 328 K at a fixed inhibitor concentration of 10^{-3} M.

The analysis of the polarization curves in Figure 9 reveals that the addition of $\text{A}_2\text{MnP}_2\text{O}_7$ (A = Li, Na, K) compounds modifies the electrochemical behavior of mild steel. While the anodic branches of the curves remain relatively parallel, the cathodic branches exhibit changes in shape. This observation suggests that the inhibitors primarily affect the corrosion rate without significantly altering the underlying corrosion mechanism.

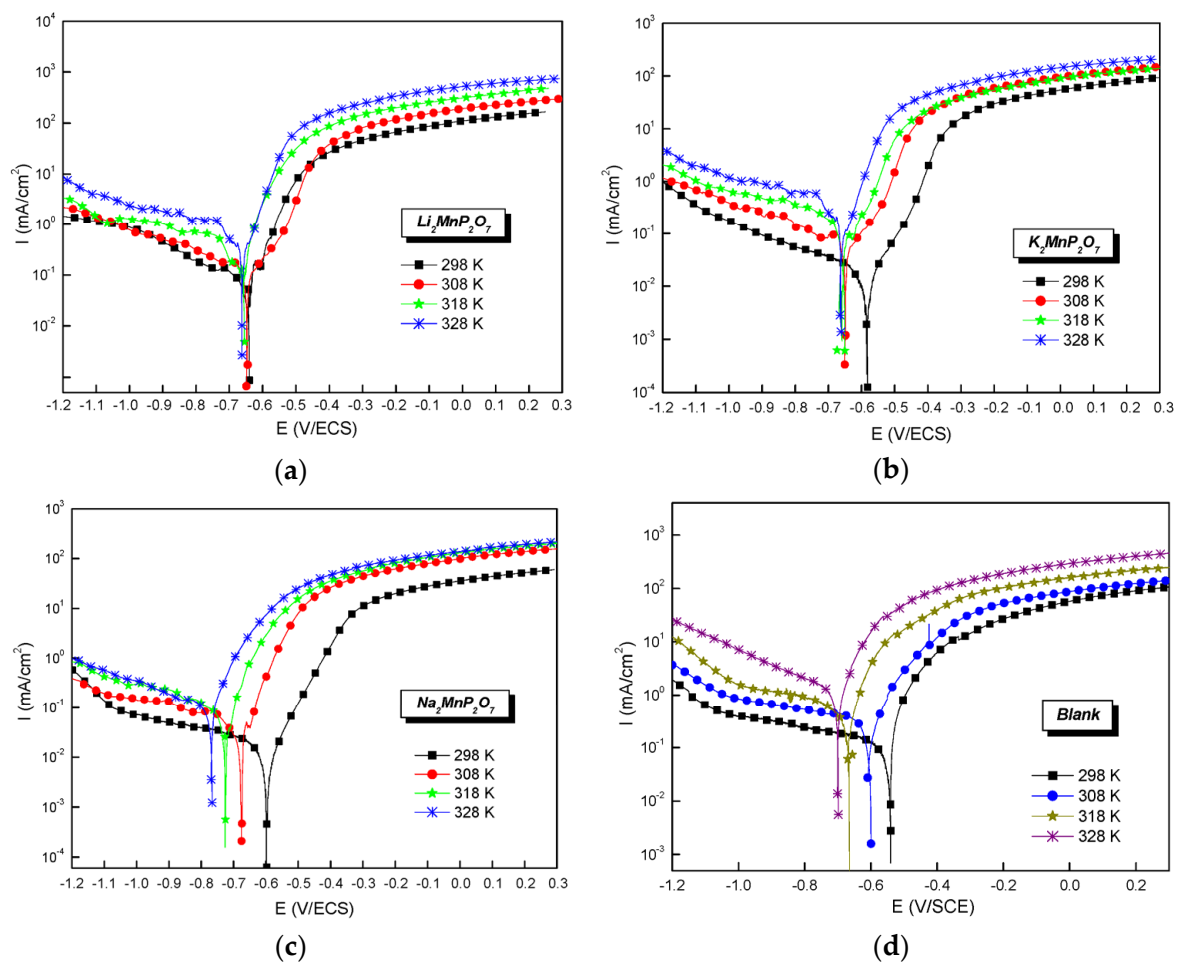


Figure 9. Effect of temperature on cathodic and anodic polarization diagrams in 3 wt.% NaCl with (a) $\text{Li}_2\text{MnP}_2\text{O}_7$, (b) $\text{K}_2\text{MnP}_2\text{O}_7$, (c) $\text{Na}_2\text{MnP}_2\text{O}_7$, and (d) the blank solution at the optimum concentrations of 10^{-3} mol/L.

Table 5 shows a slight increase in corrosion current density (i_{corr}) and a corresponding decrease in inhibition efficiency as the temperature is elevated from 298 K to 328 K. This trend confirms that the rate of metal dissolution accelerates with increasing temperature, likely due to enhanced molecular motion and a potential decrease in the stability of the protective inhibitor film.

Table 5. Polarization parameters of mild steel in 3 wt.% NaCl in the presence and absence of investigated compounds at 10^{-3} mol/L at different temperatures.

Compounds	Temp. (K)	$-E_{corr}$ (mV/SCE)	i_{corr} ($\mu\text{A cm}^{-2}$)	η %
3 wt.% NaCl	298	559	464	-
	308	594	758	-
	318	664	1353	-
	328	696	2170	-
$\text{Li}_2\text{MnP}_2\text{O}_7$	298	641	62	86.6
	308	613	117	84.5
	318	653	246	81.8
	328	660	468	78.4
$\text{K}_2\text{MnP}_2\text{O}_7$	298	580	60	87.0
	308	644	118	84.4
	318	651	245	81.8
	328	659	472	78.2
$\text{Na}_2\text{MnP}_2\text{O}_7$	298	597	54	88.3
	308	672	105	86.1
	318	733	223	83.5
	328	758	412	81.0

2.3.6. Scanning Electron Microscopy

Scanning electron microscopy (SEM) was employed to examine the surface morphology of mild steel samples exposed to 3 wt.% NaCl solutions with and without the inhibitors. The inhibitors $\text{K}_2\text{MnP}_2\text{O}_7$, $\text{Li}_2\text{MnP}_2\text{O}_7$, and $\text{Na}_2\text{MnP}_2\text{O}_7$ exhibited good inhibition efficiencies of 87%, 86.6%, and 88.3%, respectively.

Figure 10 reveals significant differences in surface morphology. The mild steel sample immersed in the solution without inhibitors displays extensive corrosion damage (Figure 10a). In contrast, the presence of $\text{A}_2\text{MnP}_2\text{O}_7$ ($\text{A} = \text{Li}, \text{Na}, \text{K}$) (Figure 10b–d) inhibitors results in a markedly improved surface with reduced signs of corrosion, such as fewer scratches. The SEM analysis confirms the adsorption of the inhibitors onto the mild steel surface, supporting the hypothesis that they form a protective layer.

These SEM observations strongly corroborate the findings from the electrochemical measurements. Together, these results demonstrate that the addition of 10^{-3} mol/L of $\text{K}_2\text{MnP}_2\text{O}_7$, $\text{Li}_2\text{MnP}_2\text{O}_7$, and $\text{Na}_2\text{MnP}_2\text{O}_7$ effectively mitigates the corrosion of mild steel in the 3 wt.% NaCl environment.

The Energy-Dispersive X-ray spectroscopy (EDS) analysis, as depicted in Figure 10, elucidated the surface chemistry of the metal when subjected to the inhibitor-treated solution, affirming the emergence of manganese (Mn) ion peaks. This observation is paramount, as Mn ions are integral to the chemical constitution of $\text{A}_2\text{MnP}_2\text{O}_7$ compounds, where A represents Li, Na, or K. Such findings substantiate the successful formation of a protective film on the surface of the steel, attributable to the unique chemical compositions of the synthesized compounds.

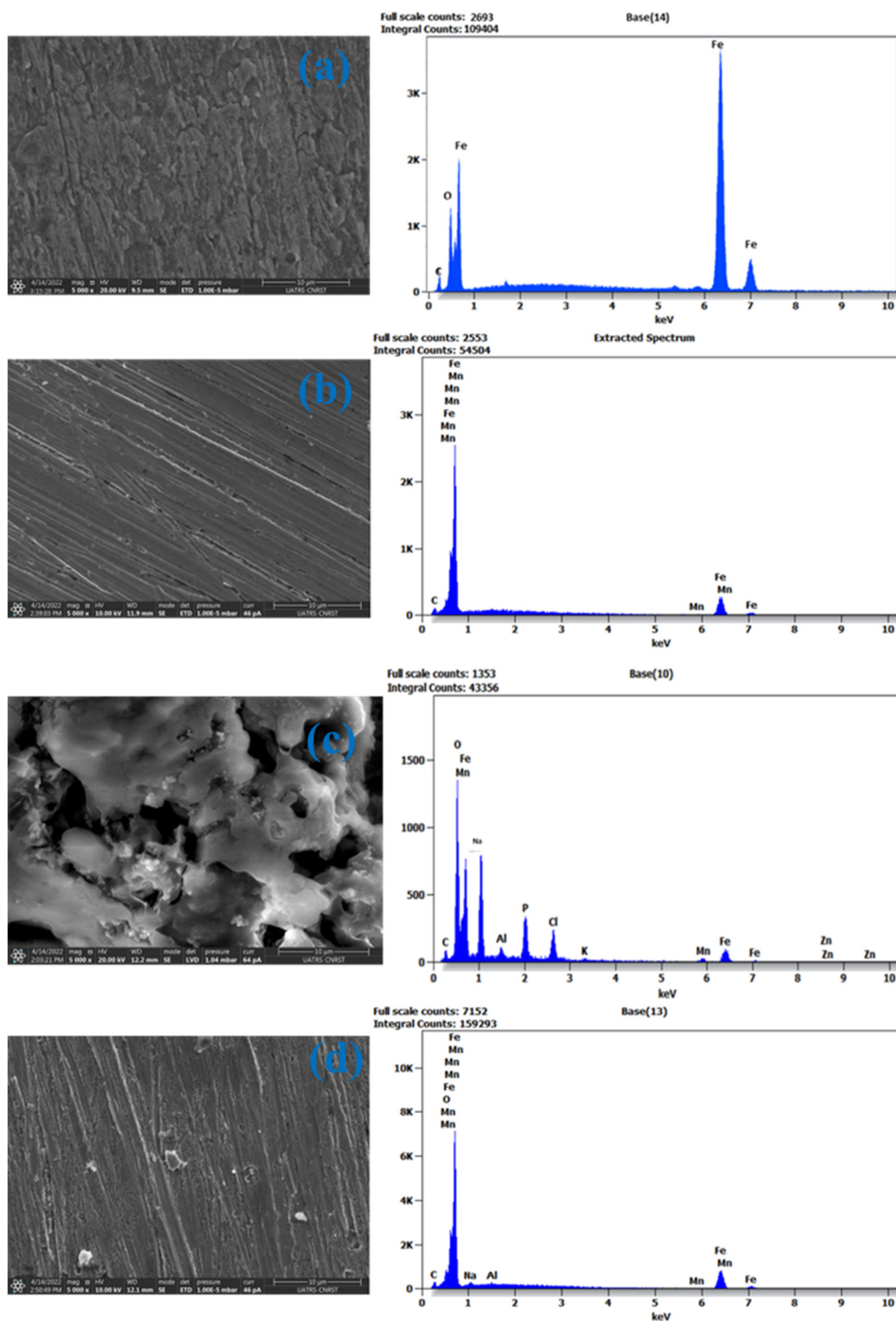


Figure 10. SEM-EDS image of mild steel after 6 h of immersion in (a) 3 wt.% NaCl solution and (b) Na₂MnP₂O₇, (c) K₂MnP₂O₇, and (d) Li₂MnP₂O₇ at 298 K.

3. Materials and Methods

3.1. Materials and Sample Preparation

The aggressive solution used in this study is 3 wt.% NaCl obtained by dissolving an appropriate amount of NaCl powder in distilled water. A range of concentrations between 10^{-6} and 10^{-3} M was prepared as well as the control solution. Samples of mild steel with a nominal chemical composition of 0.17 wt.% C, 0.37 wt.% manganese, 0.20 wt.% Si, 0.03 wt.%

S, and 0.01 wt.% P and Fe were used for electrochemical experiments; steel samples were used with an exposed area of 1.0 cm² to the corrosive medium. Before use, the substrates were abraded with different grades of emery papers from 80 to 2000 grit, rinsed with distilled water, degreased with ethanol, and dried at room temperature.

3.2. Synthesis of A₂MnP₂O₇ Compounds

The synthesis of A₂MnP₂O₇ compounds, where A signifies Li, Na, or K, was accomplished through a solid-state reaction approach. The precursor materials comprised manganese carbonate (MnCO₃, 0.5 mol), diammonium hydrogen phosphate ((NH₄)₂HPO₄, 1.0 mol), and A₂CO₃ (0.5 mol)—with “A” denoting the monovalent cation of interest. These components were meticulously combined in precise stoichiometric ratios within an agate mortar to ensure a uniform mixture. The blend underwent a sequential thermal treatment within alumina crucibles, delineated by several distinct phases: Initially, the mixture was heated to 250 °C for a duration of 10 h to facilitate the removal of water. Subsequently, the temperature was elevated to 400 °C for 3 h to potentially eliminate any residual ammonia (NH₃) and water (H₂O). This was followed by an increase in temperature to 600 °C, maintained for 4 h, aimed at expelling carbon dioxide (CO₂). The culmination of the thermal treatment involved a calcination process, with temperatures ranging from 700 °C to 800 °C over 5 h, and ultimately stabilized at 800 °C for the final hour. The precise temperature settings during the final calcination step were adjusted according to the specific monovalent cation being incorporated into the compound.

3.3. Characterization

X-ray Diffraction (XRD): The structural analysis of the synthesized compounds was performed using an EXPERT diffractometer (Philips Expert, Amsterdam, the Netherlands) equipped with a copper anticathode ($\lambda_{\text{K}\alpha\text{Cu}} = 1.5406 \text{ \AA}$). The analysis was carried out at Ibn Tofail University, Kenitra, Morocco.

Fourier Transform Infrared Spectroscopy (FTIR): Vibrational modes were investigated using a BRUKER TENSOR spectrometer (Bruker, Karlsruhe, Germany) with ATR infrared in the range of 400–1600 cm⁻¹. The analysis was carried out at Ibn Tofail University, Kenitra, Morocco.

Raman Spectroscopy: Raman spectra were obtained at room temperature using a BRUKER instrument (Bruker, Karlsruhe, Germany) with an argon ion laser excitation source ($\lambda = 532 \text{ nm}$). Spectra were recorded within the 1600–200 cm⁻¹ range with a spectral resolution of 3–5 cm⁻¹. The analysis was carried out at Ibn Tofail University, Kenitra, Morocco.

Scanning Electron Microscopy (SEM): SEM is a powerful tool for investigating surface morphology at high magnifications. It provides detailed images of surface features, including cracks, defects, and corrosion damage. SEM utilizes a focused beam of electrons to scan the surface of a sample. The interaction of electrons with the sample generates various signals, including secondary electrons, which provide topographical information. The high resolution and depth of field offered by SEM make it invaluable for analyzing the effects of corrosion processes, the efficacy of surface treatments, and the distribution of protective layers. The surface morphology analysis was conducted using a QUATTRO S-FEG-Thermofisher SEM (CNRST laboratories, Morocco) operating at a 10 kV accelerating voltage and a 2500× magnification.

3.4. Electrochemical Measurements

The electrochemical characterization involved potentiodynamic polarization and electrochemical impedance spectroscopy (EIS). A three-electrode cell was employed, consisting of a saturated calomel electrode (SCE) as the reference electrode, a platinum grid as the counter electrode, and a mild steel working electrode (1 cm² exposed area). Electrodes were connected to a VoltaMaster 4 potentiostat/galvanostat. Before the measurements, the

mild steel working electrode was immersed in the 3 wt.% NaCl test solution (with varying inhibitor concentrations) for 30 min to establish a steady-state open circuit potential.

Potentiodynamic polarization curves reveal the relationship between applied potential and corrosion current density. By analyzing these curves, one can determine corrosion rates, identify inhibition mechanisms (anodic, cathodic, or mixed), and assess the effectiveness of corrosion inhibitors in mitigating the corrosion process. Potentiodynamic curves were obtained by applying a continuous potential sweep at a rate of 1 mV/s. The potential range for the measurements was set between -1200 mV and 200 mV (vs. SCE reference electrode).

Electrochemical impedance spectroscopy (EIS) is a powerful technique for investigating corrosion processes and evaluating corrosion inhibitors. By applying small AC potential disturbances and measuring the resulting current response, EIS provides insights into interfacial processes, corrosion rates, and the formation of protective films on metal surfaces. This non-destructive technique offers valuable information about the kinetics and mechanisms of corrosion and inhibitor action. Electrochemical impedance measurements were carried out under the same conditions as the potentiodynamic polarization experiments. Data were acquired within a frequency range of 100 kHz to 100 mHz, applying a sinusoidal disturbance potential of 10 mV.

4. Conclusions

This study successfully synthesized phosphate-based compounds $A_2MnP_2O_7$ ($A = Li, Na, K$) using a dry method. Comprehensive characterization employing X-ray diffraction (XRD), Fourier Transform Infrared (FTIR), and Raman spectroscopy provided detailed insights into their structural features. FTIR and Raman analyses confirmed the presence of the pyrophosphate group and the non-linearity of the P-O-P bridge. A factor group analysis further elucidated the vibrational modes, revealing the existence of multiple Raman-active Ag modes and infrared-active Au modes within each of the synthesized compounds.

Crucially, the synthesized $K_2MnP_2O_7$, $Li_2MnP_2O_7$, and $Na_2MnP_2O_7$ compounds exhibited significant corrosion inhibition properties for mild steel in a 3 wt.% NaCl solution. Polarization curves demonstrated their role as mixed-type inhibitors with a pronounced cathodic effect. A key finding was the direct relationship between inhibitor concentration and inhibition efficiency, while a rise in temperature led to a decrease in efficiency. Among the tested compounds, $Na_2MnP_2O_7$ displayed the highest inhibition efficiency, reaching a value of 88.3%.

The adsorption behavior of these inhibitors on the mild steel surface was found to adhere to the Langmuir isotherm model. This suggests the formation of a protective monolayer on the metal surface, effectively hindering corrosive interactions. Scanning electron microscopy (SEM) provided direct visual evidence of this protective effect. SEM images revealed a notable improvement in surface morphology after the addition of $K_2MnP_2O_7$, $Li_2MnP_2O_7$, and $Na_2MnP_2O_7$, further supporting their role in mitigating corrosion.

In summary, these findings highlight the potential of the synthesized phosphate-based compounds as promising corrosion inhibitors for mild steel in saline environments. Future research will explore their performance in various media and investigate potential synergistic effects with other corrosion mitigation strategies.

Author Contributions: Conceptualization, methodology, validation, formal analysis, data curation, investigation, and writing—original draft preparation, O.M., H.E.H. and H.L.; resources, software, and investigation, M.O. and R.K.; visualization, supervision, project administration, and writing—review and editing, M.E.T., H.L. and M.H.; investigation, data curation, and writing—review and editing, K.B. and S.A. All authors have read and agreed to the published version of the manuscript.

Funding: This research was not funded by any external funding.

Data Availability Statement: The data used for making the reported results and analysis are available upon formal request.

Conflicts of Interest: The authors declare no conflicts of interest.

References

1. Jouini, A.; Gâcon, J.C.; Ferid, M.; Trabelsi-Ayadi, M. Luminescence and Scintillation Properties of Praseodymium Poly and Diphosphates. *Opt. Mater.* **2003**, *24*, 175–180. [[CrossRef](#)]
2. Wisniewski, D.; Wojtowicz, A.J.; Drozdowski, W.; Farmer, J.M.; Boatner, L.A. $\text{Rb}_3\text{Lu}(\text{PO}_4)_2\text{:Ce}$ and $\text{Cs}_3\text{Lu}(\text{PO}_4)_2\text{:Ce}$ —New Promising Scintillator Materials. *Cryst. Res. Technol.* **2003**, *38*, 275–282. [[CrossRef](#)]
3. Yuan, J.L.; Wang, J.; Xiong, D.B.; Zhao, J.T.; Fu, Y.B.; Zhang, G.B.; Shi, C.S. Potential PDP Phosphors with Strong Absorption around 172 nm: Rare Earth Doped NaLaP_2O_7 and NaGdP_2O_7 . *J. Lumin.* **2007**, *126*, 717–722. [[CrossRef](#)]
4. Carvajal, J.J.; Parreu, I.; Solé, R.; Solans, X.; Díaz, F.; Aguiló, M. Growth and Structural Characterization of $\text{Rb}_3\text{Yb}_2(\text{PO}_4)_3$: A New Material for Laser and Nonlinear Optical Applications. *Chem. Mater.* **2005**, *17*, 6746–6754. [[CrossRef](#)]
5. Vitiš, G.; Kanepe, Z.; Vitiš, A.; Ronis, J.; Dindūne, A.; Lūsis, A. Structural and Conductivity Studies in LiFeP_2O_7 , LiScP_2O_7 , and NaScP_2O_7 . *J. Solid State Electrochem.* **2000**, *4*, 146–152. [[CrossRef](#)]
6. Belharouak, I.; Parent, C.; Gravereau, P.; Chaminade, J.P.; Flem, G.L.; Moine, B. Luminescent Properties of Silver(I) Diphosphate of Compositions $\text{Na}_{2-x}\text{Ag}_x\text{ZnP}_2\text{O}_7$. *J. Solid State Chem.* **2000**, *149*, 284–291. [[CrossRef](#)]
7. Hamani, H.; Douadi, T.; Daoud, D.; Al-Noaimi, M.; Rikkouh, R.A.; Chafaa, S. 1-(4-Nitrophenyl)-1-(Phenylhydrazono)-Propan-2-One as Corrosion Inhibitor for Mild Steel in 1M HCl Solution: Weight Loss, Electrochemical, Thermodynamic and Quantum Chemical Studies. *J. Electroanal. Chem.* **2017**, *801*, 425–438. [[CrossRef](#)]
8. Issaadi, S.; Douadi, T.; Zouaoui, A.; Chafaa, S.; Khan, M.A.; Bouet, G. Novel Thiophene Symmetrical Schiff Base Compounds as Corrosion Inhibitor for Mild Steel in Acidic Media. *Corros. Sci.* **2011**, *53*, 1484–1488. [[CrossRef](#)]
9. Aloui, S.; Forsal, I.; Sfaira, M.; Touhami, M.E.; Taleb, M.; Baba, M.F.; Daoudi, M. New Mechanism Synthesis of 1,4-Benzothiazine and Its Inhibition Performance on Mild Steel in Hydrochloric Acid. *Port. Electrochim. Acta* **2009**, *27*, 599–613. [[CrossRef](#)]
10. Ghailane, T.; Balkhmima, R.A.; Ghailane, R.; Souizi, A.; Touri, R.; Ebn Touhami, M.; Marakchi, K.; Komiha, N. Experimental and Theoretical Studies for Mild Steel Corrosion Inhibition in 1M HCl by Two New Benzothiazine Derivatives. *Corros. Sci.* **2013**, *76*, 317–324. [[CrossRef](#)]
11. Panda, A.K.; Purohit, A.K.; Upadhyay, A.; Sahoo, M.K.; Kar, P.K. Corrosion Inhibition Studies on Mild Steel in HCl by a Newly Synthesized Benzil Monohydrazone Based Schiff Base. *J. Indian Chem. Soc.* **2021**, *98*, 100245. [[CrossRef](#)]
12. Bayol, E.; Gürten, T.; Gürten, A.A.; Erbil, M. Interactions of Some Schiff Base Compounds with Mild Steel Surface in Hydrochloric Acid Solution. *Mater. Chem. Phys.* **2008**, *112*, 624–630. [[CrossRef](#)]
13. Medupin, R.O.; Ukoba, K.O.; Yoro, K.O.; Jen, T.-C. Sustainable Approach for Corrosion Control in Mild Steel Using Plant-Based Inhibitors: A Review. *Mater. Today Sustain.* **2023**, *22*, 100373. [[CrossRef](#)]
14. Chami, A.; Benabbou, R.; Taleb, M.; Rais, Z.; El Haji, M. Inhibition of Corrosion of Steel in 1 M HCl Solution by Polyphenol Extract: Application for Steel Used in the Automotive Industry in Morocco. *Moroc. J. Chem.* **2023**, *11*, 623–644. [[CrossRef](#)]
15. Salim, A.; Hamham, S.; Ahmed, M.; El Harrari, S.; El mazouzi, S.; Naimi, Y. Study of the Inhibiting Efficiency of the Corrosion Inhibitor (Prop-2-Yn-1-ol, Methyloxirane) of Mild Steel in the Chemical Pickling (18.5% HCl). *Moroc. J. Chem.* **2023**, *11*, 718–728. [[CrossRef](#)]
16. Hamdouch, A.; Anejjar, A.; Bijla, L.; Gharby, S.; Asdadi, A.; Chebli, B.; Salghi, R.; Idrissi Hassani, L.M. Corrosion Inhibition of Carbon Steel by Vitex Agnus Castus Leaves Essential Oils from the Oasis of Tata. *Moroc. J. Chem.* **2023**, *11*, 105–118. [[CrossRef](#)]
17. Ebenso, E.; Verma, C.; Olasunkanmi, L.; Akpan, E.; Verma, D.; Lgaz, H.; Guo, L.; Kaya, S.; Quraishi, M. Molecular Modelling of Compounds Used for Corrosion Inhibition Studies: A Review. *Phys. Chem. Chem. Phys.* **2021**, *23*, 19987–20027. [[CrossRef](#)]
18. Macedo, R.G.M.d.A.; Marques, N.d.N.; Tonholo, J.; Balaban, R.d.C. Water-Soluble Carboxymethylchitosan Used as Corrosion Inhibitor for Carbon Steel in Saline Medium. *Carbohydr. Polym.* **2019**, *205*, 371–376. [[CrossRef](#)]
19. Nardeli, J.V.; Fugivara, C.S.; Taryba, M.; Pinto, E.R.P.; Montemor, M.F.; Benedetti, A.V. Tannin: A Natural Corrosion Inhibitor for Aluminum Alloys. *Prog. Org. Coat.* **2019**, *135*, 368–381. [[CrossRef](#)]
20. Dehghani, A.; Bahlakeh, G.; Ramezanzadeh, B.; Ramezanzadeh, M. Potential of Borage Flower Aqueous Extract as an Environmentally Sustainable Corrosion Inhibitor for Acid Corrosion of Mild Steel: Electrochemical and Theoretical Studies. *J. Mol. Liq.* **2019**, *277*, 895–911. [[CrossRef](#)]
21. Haleem, S.M.A.E.; Wanees, S.A.E.; Aal, E.E.A.E.; Diab, A. Environmental Factors Affecting the Corrosion Behavior of Reinforcing Steel. IV. Variation in the Pitting Corrosion Current in Relation to the Concentration of the Aggressive and the Inhibitive Anions. *Corros. Sci.* **2010**, *52*, 1675–1683. [[CrossRef](#)]
22. Jamil, H.E.; Shrirri, A.; Boulif, R.; Bastos, C.; Montemor, M.F.; Ferreira, M.G.S. Electrochemical Behaviour of Amino Alcohol-Based Inhibitors Used to Control Corrosion of Reinforcing Steel. *Electrochim. Acta* **2004**, *49*, 2753–2760. [[CrossRef](#)]
23. Nahali, H.; Dhoubi, L.; Idrissi, H. Effect of Phosphate Based Inhibitor on the Threshold Chloride to Initiate Steel Corrosion in Saturated Hydroxide Solution. *Constr. Build. Mater.* **2014**, *50*, 87–94. [[CrossRef](#)]
24. Bastidas, D.M.; Martin, U.; Bastidas, J.M.; Ress, J. Corrosion Inhibition Mechanism of Steel Reinforcements in Mortar Using Soluble Phosphates: A Critical Review. *Materials* **2021**, *14*, 6168. [[CrossRef](#)] [[PubMed](#)]
25. Elhafiane, F.Z.; Khaoulaf, R.; Harcharras, M.; Brouzi, K. Synthesis, Crystal Structure, Vibrational Spectroscopy and Electrochemical Investigations of a New Acidic Metal Pyrophosphate $\text{NiK}_{1.18}\text{N}_{0.82}(\text{H}_2\text{P}_2\text{O}_7)_2 \cdot 2\text{H}_2\text{O}$. *J. Mol. Struct.* **2021**, *1245*, 131234. [[CrossRef](#)]
26. Khmias, J.; Kerroum, Y.; Aoufir, Y.E.; Guenbour, A.; Bellaouchou, A.; Zarrouk, A.; Assani, A.; Saadi, M.; Ammari, L.E. Synthesis of Novel Orthophosphate Compound $\text{AgSr}_4\text{Cu}_{4.5}(\text{PO}_4)_6$: Characterization and Anticorrosion Activities. *Chem. Data Collect.* **2022**, *41*, 100912. [[CrossRef](#)]

27. Hasumi, M.; Taniguchi, I. Synthesis and Characterization of $\text{Li}_2\text{MnP}_2\text{O}_7/\text{C}$ Composite by a Combination of Spray Pyrolysis and Wet Ball Milling Followed by Annealing. *Mater. Lett.* **2014**, *134*, 202–205. [[CrossRef](#)]
28. Kaoua, S.; Krimi, S.; Péchev, S.; Graveriau, P.; Chaminade, J.-P.; Couzi, M.; Jazouli, A.E. Synthesis, Crystal Structure, and Vibrational Spectroscopic and UV-Visible Studies of $\text{Cs}_2\text{MnP}_2\text{O}_7$. *J. Solid State Chem.* **2013**, *198*, 379–385. [[CrossRef](#)]
29. Ye, Y.; Zou, Y.; Jiang, Z.; Yang, Q.; Chen, L.; Guo, S.; Chen, H. An Effective Corrosion Inhibitor of N Doped Carbon Dots for Q235 Steel in 1 M HCl Solution. *J. Alloys Compd.* **2020**, *815*, 152338. [[CrossRef](#)]
30. Hirschorn, B.; Orazem, M.E.; Tribollet, B.; Vivier, V.; Frateur, I.; Musiani, M. Determination of Effective Capacitance and Film Thickness from Constant-Phase-Element Parameters. *Electrochim. Acta* **2010**, *55*, 6218–6227. [[CrossRef](#)]
31. Bouammali, H.; Jama, C.; Bekkouch, K.; Aouniti, A.; Hammouti, B.; Bentiss, F. Anticorrosion Potential of Diethylenetriamine-pentakis (Methylphosphonic) Acid on Carbon Steel in Hydrochloric Acid Solution. *J. Ind. Eng. Chem.* **2015**, *26*, 270–276. [[CrossRef](#)]
32. Shahryari, Z.; Gheisari, K.; Yeganeh, M.; Ramezanzadeh, B. Corrosion Mitigation Ability of Differently Synthesized Polypyrrole (PPy- FeCl_3 & PPy-APS) Conductive Polymers Modified with Na_2MoO_4 on Mild Steel in 3.5% NaCl Solution: Comparative Study and Optimization. *Corros. Sci.* **2021**, *193*, 109894. [[CrossRef](#)]
33. Abdel-Gaber, A.M.; Abd-El-Nabey, B.A.; Sidahmed, I.M.; El-Zayady, A.M.; Saadawy, M. Inhibitive Action of Some Plant Extracts on the Corrosion of Steel in Acidic Media. *Corros. Sci.* **2006**, *48*, 2765–2779. [[CrossRef](#)]
34. Flis, J.; Zakroczyński, T. Impedance Study of Reinforcing Steel in Simulated Pore Solution with Tannin. *J. Electrochem. Soc.* **1996**, *143*, 2458–2464. [[CrossRef](#)]
35. Wang, D.-Y.; Nie, B.-L.; Li, H.-J.; Zhang, W.-W.; Wu, Y.-C. Anticorrosion Performance of Grape Seed Proanthocyanidins Extract and Tween-80 for Mild Steel in Hydrochloric Acid Medium. *J. Mol. Liq.* **2021**, *331*, 115799. [[CrossRef](#)]
36. Fouda, A.S.; Ismail, M.A.; Abou-shahba, R.M.; Husien, W.A.; EL-Habab, E.S.; Abousalem, A.S. Experimental and Computational Chemical Studies on the Cationic Furanyl nicotinamidines as Novel Corrosion Inhibitors in Aqueous Solutions. *Chin. J. Chem. Eng.* **2020**, *28*, 477–491. [[CrossRef](#)]
37. Alharthi, N.H.; El-Hashemy, M.A.; Derafa, W.M.; Althobaiti, I.O.; Altaieb, H.A. Corrosion Inhibition of Mild Steel by Highly Stable Polydentate Schiff Base Derived from 1,3-Propanediamine in Aqueous Acidic Solution. *J. Saudi Chem. Soc.* **2022**, *26*, 101501. [[CrossRef](#)]
38. Al-Amiery, A.A.; Shaker, L.M.; Kadhum, A.H.; Takriff, M.S. Exploration of Furan Derivative for Application as Corrosion Inhibitor for Mild Steel in Hydrochloric Acid Solution: Effect of Immersion Time and Temperature on Efficiency. *Mater. Today Proc.* **2021**, *42*, 2968–2973. [[CrossRef](#)]
39. Fouda, A.S.; Ellithy, A.S. Inhibition Effect of 4-Phenylthiazole Derivatives on Corrosion of 304L Stainless Steel in HCl Solution. *Corros. Sci.* **2009**, *51*, 868–875. [[CrossRef](#)]

Disclaimer/Publisher's Note: The statements, opinions and data contained in all publications are solely those of the individual author(s) and contributor(s) and not of MDPI and/or the editor(s). MDPI and/or the editor(s) disclaim responsibility for any injury to people or property resulting from any ideas, methods, instructions or products referred to in the content.